Faraday Discussions

Cite this: *Faraday Discuss.*, 2014, **171**, 113

PAPER

View Article Online
View Journal | View Issue

The sensitivities of high-harmonic generation and strong-field ionization to coupled electronic and nuclear dynamics

Denitsa Baykusheva,[a] Peter M. Kraus,[a] Song Bin Zhang,[bc] Nina Rohringer[bc] and Hans Jakob Wörner[a]

Received 21st February 2014, Accepted 14th April 2014
DOI: 10.1039/c4fd00018h

The sensitivities of high-harmonic generation (HHG) and strong-field ionization (SFI) to coupled electronic and nuclear dynamics are studied, using the nitric oxide (NO) molecule as an example. A coherent superposition of electronic and rotational states of NO is prepared by impulsive stimulated Raman scattering and probed by simultaneous detection of HHG and SFI yields. We observe a fourfold higher sensitivity of high-harmonic generation to electronic dynamics and attribute it to the presence of inelastic quantum paths connecting coherently related electronic states [Kraus *et al.*, *Phys. Rev. Lett.* **111**, 243005 (2013)]. Whereas different harmonic orders display very different sensitivities to rotational or electronic dynamics, strong-field ionization is found to be most sensitive to electronic motion. We introduce a general theoretical formalism for high-harmonic generation from coupled nuclear-electronic wave packets. We show that the unequal sensitivities of different harmonic orders to electronic or rotational dynamics result from the angle dependence of the photorecombination matrix elements which encode several autoionizing and shape resonances in the photoionization continuum of NO. We further study the dependence of rotational and electronic coherences on the intensity of the excitation pulse and support the observations with calculations.

1 Introduction

The motion of electrons determines the basic properties of atoms and molecules. Since electronic motion occurs on femto- down to attosecond time scales, its characterization and control depends on the availability of ultrafast radiation sources combined with efficient detection techniques. Recent advances in this direction include the development of attosecond streaking, which enabled the measurement of Auger decay times[1] and photoemission delays.[2] Resolving

[a]*ETH Zürich, Laboratory of Physical Chemistry, 8093 Zurich, Switzerland. E-mail: woerner@phys.chem.ethz.ch*
[b]*Max Planck Institute for the Physics of Complex Systems, 01187 Dresden, Germany*
[c]*Center for Free-Electron Laser Science, 22607 Hamburg, Germany*

electron dynamics has also been approached employing interferometric techniques,[3] transient absorption[4–6] or strong-field ionization (SFI).[7,8] The methods enumerated so far, however, operate on highly excited states or ionic species. Recently, we have reported the first experiment measuring an electronic wave packet involving the ground electronic state of a neutral molecule.[9]

In the past, the possibility to study coherent electronic wave packets by high-harmonic generation (HHG) has been subject to an intensive theoretical investigation.[10–13] Our new pump–probe technique,[9] relying on impulsive stimulated Raman scattering (ISRS) and HHG, provides unprecedented sensitivity and is thus ideal to study weakly allowed electronic transitions and their coupling to the other motional degrees of freedom in the time domain. The technique is directly sensitive to the electronic coherence and its evolution due to previously unobserved HHG cross channels connecting distinct but coherently related states.[9] The method differs from previous applications of high-harmonic spectroscopy,[14] where a photoexcited molecular wave packet was followed by HHG. The latter technique enabled the resolution of the conical intersection dynamics in NO_2[15,16,17] and the photodissociation of CH_3I and CF_3I[18] but was blind to the cross-channels that reveal the electronic coherence. The present technique also differs from previous measurements of electronic dynamics in molecular ions by HHG[19–22] in the sense that the latter are also blind to electronic coherence between the levels of the cation.

The study of electronic dynamics further requires the development of theoretical frameworks predicting the interaction of a system with an intense laser field and the HHG probe process. Existing methods are based on the density-matrix formalism[23–25] or S-matrix-based approaches.[26–28] Quantitative rescattering theory,[29] which expresses the HHG intensity as a product of a returning electron wave packet and photoionization molecular-frame matrix elements,[30,31] is another popular approach that has been applied to a wide range of diatomic molecules and even polyatomic species.[32]

In the present article, we extend our previous study of electronic wave packets in aligned molecules[9] to longer pump–probe delays, and demonstrate how the complete quantum-level structure of two electronic states can be determined by Fourier transforming the HHG or SFI signals. This approach also enables us to resolve different types of coherences in the frequency domain: rotational, electronic and mixed coherences. We directly compare the sensitivities of high-harmonic generation and strong-field ionization to the electronic dynamics and find that the sensitivity of the former exceeds that of the latter by a factor of $\sim$4. We develop a closed-form theoretical treatment to describe both the excitation and the probing steps. The comparison of theory and experiment shows that the angle dependence of the photorecombination matrix elements is the origin of the different sensitivities of the various harmonic orders to the rotational motion. Several autoionizing and shape resonances in the photoionization continuum of NO around 14 eV are mapped into a pronounced signal modulation at the rotational revivals. Finally, we present a systematic study of the pump-pulse intensity which shows that the rotational excitation saturates at lower intensities than the electronic excitation.

2 Theory

2.1 Field-free rotational structure

The open-shell nature of the ground-state electronic configuration of the NO radical gives rise to two fine-structure components, with $^2\Pi_{1/2}$ being the ground-state and $^2\Pi_{3/2}$ lying $\sim$123 cm^{-1} higher in energy.[33] The field-free Hamiltonian is

$$\hat{H}_0 = \hat{H}_{\rm rot} + \hat{H}_{\rm SO} = hcB(\mathbf{J}-\mathbf{L}-\mathbf{S})^2 - hcA\mathbf{L}\cdot\mathbf{S}, \quad (1)$$

whereby $B \approx 1.6961$ cm^{-1} and $A \approx 123.1314$ cm^{-1} designate the ground-state rotational and the spin–orbit coupling constant,[33] respectively. **L** and **S** stand for the total orbital and spin angular momentum operators, whereas the total angular momentum operator exclusive of nuclear degrees of freedom is denoted by **J**. Provided that the rotational excitation is low, Hund's coupling scheme (a) is applicable, in which case one uses the quantum numbers Λ, Σ and Ω to quantify the projections of **L**, **S** and **J** on the molecule-fixed axis. In this limit, it is convenient to adopt the parity-adapted basis set[34] defined by

$$|J|\Omega|M\varepsilon\rangle = \frac{1}{\sqrt{2}}[|J,|\Omega|,M\rangle + \varepsilon|J,-|\Omega|,M\rangle], \quad (2)$$

wherein $\varepsilon = \pm 1$ represents a symmetry index related to the total parity of the wave function p as $p = \varepsilon(-1)^{J-1/2}$. M quantifies the projection of the total angular momentum vector **J** on the reference axis in the laboratory frame and is conserved in the present experiment. The eigenfunctions $|J,\Omega,M\rangle$ relate to the elements of the Wigner rotational matrix[35] as

$$\langle \phi,\theta,\chi|J,\Omega,M\rangle \equiv \sqrt{\frac{2J+1}{4\pi}} D^{J*}_{M\Omega}(\phi,\theta,\chi=0), \quad (3)$$

where (ϕ,θ,χ) are the Euler angles defining the orientation of the body-fixed frame with respect to the lab frame. The Euler angle χ is redundant for a linear molecule and is therefore set to zero according to the convention used in ref. 34. Under the assumption that interactions with higher-lying Σ-electronic states[36] (Λ-*doubling*) can be neglected, the wave functions corresponding to the two values of ε can be treated as degenerate. In the case of the NO molecule, $|\Omega|$ assumes the values $\frac{1}{2}$ and $\frac{3}{2}$, and the matrix representation of the field-free Hamiltonian in eqn (1) becomes

$$\hat{\mathbf{H}}_0 = \begin{pmatrix} B\left(J-\frac{1}{2}\right)\left(J+\frac{3}{2}\right) & -B\sqrt{\left(J-\frac{1}{2}\right)\left(J+\frac{3}{2}\right)} \\ -B\sqrt{\left(J-\frac{1}{2}\right)\left(J+\frac{3}{2}\right)} & A-2B+B\left(J-\frac{1}{2}\right)\left(J+\frac{3}{2}\right). \end{pmatrix} \quad (4)$$

Diagonalizing the above expression, one obtains for the eigenbasis:

$$\begin{pmatrix} |JM\varepsilon;1\rangle \\ |JM\varepsilon;2\rangle \end{pmatrix} = \begin{pmatrix} a_J & b_J \\ -b_J & a_J \end{pmatrix} \begin{pmatrix} |J\,\frac{1}{2}M\varepsilon\rangle \\ |J\,\frac{3}{2}M\varepsilon\rangle \end{pmatrix}, \quad (5)$$

wherein the coefficients a_J and b_J are functions of the rotational and spin–orbit constants and obey the relationship $a_J^2 + b_J^2 = 1$. The eigenstates in this new basis are labelled F_1 and F_2 and the corresponding eigenenergies are given by

$$\begin{cases} E_{F_1} = B\left(J-\frac{1}{2}\right)\left(J+\frac{3}{2}\right) - \sqrt{B^2\left(J+\frac{1}{2}\right)^2 + \frac{A(A-4B)}{4}} + \frac{A-2B}{2} \\ E_{F_2} = B\left(J-\frac{1}{2}\right)\left(J+\frac{3}{2}\right) + \sqrt{B^2\left(J+\frac{1}{2}\right)^2 + \frac{A(A-4B)}{4}} + \frac{A-2B}{2} \end{cases}. \quad (6)$$

The limit of a pure Hund's coupling case (a) is characterized by the values $a_J = 1$ and $b_J = 0$ (or *vice versa*). Here, $a_J \sim 1$ and $b_J \sim 0$ for low values of J, thus the F_1 state in NO is dominated by the $^2\Pi_{1/2}$ fine-structure component, whereas the F_2 state is $^2\Pi_{3/2}$-dominated.

2.2 Pump pulse interaction: electronic and rotational Raman transitions

When subject to a short†, intense non-resonant laser pulse, the time evolution of the system obeys the Hamiltonian

$$\hat{H}_{\mathrm{M-L}}(t) = \hat{H}_0 + \hat{H}_{\mathrm{pump}}(t), \quad (7)$$

where the term $\hat{H}_{\mathrm{pump}}(t)$ conveys the interaction between the molecule and the incident electromagnetic field. The linearly polarized pump pulse is modelled as a Gaussian function in the temporal domain

$$\vec{\varepsilon}_{pu}(t) = \hat{\varepsilon}_{pu}\varepsilon_{pu}(t)\cos(\omega_0 t) = \hat{\varepsilon}_{pu}\varepsilon_{pu,0}e^{-2\ln 2(t/\tau_{pu})^2}\cos(\omega_0 t), \quad (8)$$

wherein $\hat{\varepsilon}_{pu}$ is a unit vector parallel to the polarization axis of the field, $\varepsilon_{pu,0}$ is the electric field amplitude, τ_{pu} denotes the duration of the pulse‡ and ω_0 is the fundamental frequency of the carrier field. In the current work, ω_0 corresponds to a wavelength of 800 nm, the pulse duration is estimated to be 60 fs and the peak intensity lies in the range $3-6 \times 10^{13}$ W cm^{-2} in the present experiments. The cycle-averaged interaction Hamiltonian reads

$$\begin{aligned} \hat{H}_{\mathrm{pump}}(t) &= -\frac{\varepsilon_{pu}^2(t)}{4}\hat{\varepsilon}_{pu}^{\mathrm{T}}\underline{\underline{\alpha}}\hat{\varepsilon}_{pu} \\ &= -\frac{\varepsilon_{pu}^2(t)}{4}\left[\frac{2}{3}\Delta\alpha\left(D_{00}^2(\phi,\theta,\chi) + \gamma\left(D_{02}^2(\phi,\theta,\chi) + D_{0-2}^2(\phi,\theta,\chi)\right)\right)\right. \\ &\quad \left. + \frac{1}{3}\Delta\alpha + \alpha_\perp\right]. \end{aligned} \quad (9)$$

In the static-field limit, the only non-trivial elements of the polarizability tensor $\underline{\underline{\alpha}}$ (evaluated in the principle axis system of the molecule) are $\alpha_\perp \equiv \alpha_{xx} = \alpha_{yy}$ and α_{zz}, with $\Delta\alpha = \alpha_{zz} - \alpha_\perp$. For NO, $\alpha_\perp = 9.715$ a.u. and $\alpha_{zz} = 15.34$ a.u.[37] The

† In this context, the term "short" signifies that the pulse duration is significantly smaller than the rotational period of the molecule.

‡ Here and in the remainder of this article, the pulse duration designates the full width at half maximum of the electric-field envelope.

orientation dependence of the interaction is encoded in the Wigner rotation matrices occurring in eqn (9). Using angular momentum algebra arguments, it can be readily proven that matrix elements involving $D^2_{00}(\phi,\theta,\chi)$ capture most of the rotational Raman transitions. The dependence of $\hat{H}_{\mathrm{pump}}$ on $D^2_{0\pm2}(\phi,\theta,\chi)$ accounts for the largest portion of the electronic-rotational Raman excitations. The parameter γ in eqn (9) quantifies the ratio between electronic and purely rotational Raman scattering and has been assigned the empirical value of 0.2.[38] The interaction with the electromagnetic field prepares the system in a superposition of coupled rotational and spin–orbit electronic states and the ensuing dynamics is dictated by

$$i\partial_t|\Phi_{J_0M_0\varepsilon_0 i_0}(t)\rangle = \hat{H}_{\mathrm{M-L}}(t)|\Phi_{J_0M_0\varepsilon_0 i_0}(t)\rangle. \tag{10}$$

In the above, the fundamental solution $|\Phi_{J_0M_0\varepsilon_0 i_0}(t)\rangle$ describes an electronic-rotational wave packet that uniquely evolves from an initially occupied eigenstate $|J_0M_0\varepsilon_0;i_0\rangle$ with $i_0 \in \{1, 2\}$ (cp. eqn (5)).[23] Exploiting the orthonormality of the functions $\{|JM_0\varepsilon;i\rangle\}$, the solution of eqn (10) can be obtained by expanding $\Phi_{J_0M_0\varepsilon_0 i_0}(t)$ in terms of the basis functions $\{|JM_0\varepsilon;i\rangle\}$

$$|\Phi_{J_0M_0\varepsilon_0 i_0}(t)\rangle = \sum_{J\varepsilon i} C_{F_i}^{J_0M_0\varepsilon_0}(J\varepsilon;t)|JM_0\varepsilon;i\rangle \tag{11}$$

and solving the resulting coupled differential equations for the expansion coefficients $\left\{C_{F_i}^{J_0M_0\varepsilon_0}(J\varepsilon;t)\right\}$ by imposing the initial condition

$$|\Phi_{J_0M_0\varepsilon_0 i_0}(t_0)\rangle = |J_0M_0\varepsilon_0;1\rangle, \tag{12}$$

i.e., the entire population resides initially in the F_1 spin–orbit component. The density matrix of the system $\rho(t)$ is formed by summing over the contributions of all initially occupied rotational states

$$\rho(t) = \sum_{J_0M_0\varepsilon_0 i_0} w_{J_0}|\Phi_{J_0M_0\varepsilon_0 i_0}(t)\rangle\langle\Phi_{J_0M_0\varepsilon_0 i_0}(t)|, \tag{13}$$

wherein $\{w_{J_0}\}$ are Boltzmann distribution coefficients corresponding to a rotational temperature of 15 K.

2.3 Calculation of the high-harmonic intensity

In this section, we describe the basic formalism for calculating the high-harmonic emission from a pure state $\Psi(\hat{R},\tau)$ exposed to the field of the probe pulse. $\hat{R}$ is a short-hand notation for the Euler angles (ϕ,θ,χ). The harmonic intensity is proportional to the square of the Fourier transform $|\vec{D}(\hat{R},\omega)|^2$ of the dipole-moment expectation value:

$$\vec{D}(\hat{R},\tau) = \langle\Psi(\hat{R},\tau)|\hat{\vec{\mu}}_{\mathrm{el}}|\Psi(\hat{R},\tau)\rangle. \tag{14}$$

In the framework of the QRS theory, the induced dipole moment representing high-harmonic emission is decomposed into a product of a returning electron wave packet $W(\omega)$ and the photorecombination cross section of the laser-field-free

continuum recombining back to the initial ground state.[29,31] For a single molecule whose orientation is defined by $\hat{R}$ with respect to the polarization axis of the driving field, the resulting expression for the dipole moment in the frequency domain reads

$$\vec{D}(\hat{R},\omega) = \sqrt{\Gamma(\hat{R})}\, W(\omega)\vec{d}_{rec}(\hat{R},\omega), \tag{15}$$

where $\Gamma(\hat{R})$ is the calculated[39] angle-dependent strong-field ionization rate. $W(\omega)$ denotes the complex spectral representation of the recombining photoelectron wave packet. The photorecombination matrix elements $\vec{d}_{rec}(\hat{R},\omega)$ are independent of the laser parameters and encode the dependence of the calculated harmonic spectra on the structure of the target.

2.4 Calculation of photorecombination matrix elements

The photoionization of NO is treated according to the method described by Lucchese *et al.*[40] and Stratmann *et al.*[41] including 10 ion-state channels up to an ionization potential of 23.5 eV and all associated interchannel couplings. Spin–orbit interaction is neglected in these calculations. The initial state is the $^2\Pi$ electronic ground state of NO, denoted as $\Psi^{(\Lambda_i)}$ and characterized by the electronic angular momentum projection quantum number $\Lambda_i = \pm 1$. Photoionization matrix elements are calculated for ionization to the $X^1\Sigma^+$-ground state of NO^+, $\Phi^{(\Lambda_f)}$, with $\Lambda_f = 0$, and the continuum photoelectron is represented in a single-center expansion in terms of the basis functions Ψ_{klm}, where k denotes the momentum and l and m are the orbital and projection quantum numbers, respectively. The photoionization dipole matrix elements assume the following form in the spherical basis

$$I_{\hat{k},\hat{n}}^{(\Lambda_i,\Lambda_f)} = \sum_{l,m,\mu} \left\langle \Psi^{(\Lambda_i)} | r_\mu | \Phi^{(\Lambda_f)} \Psi_{klm} \right\rangle Y_{l,m}^*(\hat{k})\, Y_{1,\mu}^*(\hat{n}), \tag{16}$$

where $\hat{n}$ denotes the polarization of light and r_μ ($\mu = 0, \pm 1$) are the spherical components of the dipole moment operator in the length gauge. The dependence of the photoionization cross section (PICS) on the orientation of the target is captured by the spherical harmonic functions $Y_{l,m}$.

2.5 High-harmonic generation from a coupled electronic-rotational wave packet

Before developing the formalism describing high-harmonic emission from a coupled electronic-rotational wave packet, we introduce two different time scales. The time scale denoted by t labels the time evolution with respect to the pump pulse, whereas τ labels the time scale of high-harmonic generation within the duration of the probe pulse. Since the wave-packet evolution described by the variable t is slow compared to the sub-femtosecond time scale of HHG described by τ, we neglect the time-evolution of the wave packet during HHG and use a parametric dependence on t in the following equations.

Building on the approach outlined by Ramakrishna and Seideman,[23] the quantum state created from the initially-occupied state $|F_{i_0};J_0M_0\varepsilon_0\rangle$ after the strong-field ionization step can be written as

$$|\Phi_{J_0M_0\varepsilon_0 i_0}(\tau;t)\rangle = \sum_{J\varepsilon i} C_{F_i}^{J_0M_0\varepsilon_0}(J\varepsilon;t)|F_i;JM_0\varepsilon\rangle e^{i\left(I_p-E_J^{F_i}\right)\tau} + \sum_{J_cM_c}\int d^3k\, C_{J_c}^{M_c}(\vec{k};\tau)|\vec{k};J_cM_c\rangle e^{iI_p\tau}, \tag{17}$$

where I_p is the vertical ionization potential of the spin-rovibronic ground state and $E_J^{F_i}$ denote the internal energies of the excited spin-rovibronic eigenstates of NO. In the above, $|\vec{k};J_cM_c\rangle = |\vec{k}\rangle \otimes |J_cM_c\rangle$ where $|\vec{k}\rangle$ denotes the electronic continuum associated with the asymptotic momentum $\vec{k}$ and $|J_cM_c\rangle$ specifies the rotational states of the ionic core. The notation $|F_i;JM_0\varepsilon\rangle$ is here to designate a rotational-electronic eigenstate of the molecular Hamiltonian that explicitly contains the complete wave function of the unpaired electron (in a single-active electron approximation). The continuum coefficients $C_{J_c}^{M_c}(\vec{k};\tau)$ are calculated using the strong-field approximation (SFA). Exploiting the fact that $E_J^{F_i}$ is negligible with respect to the magnitude of the ionization potential I_p, eqn (14), (13) and (17) can be combined to yield an expression for the induced dipole moment $d(\tau;t)$:

$$d(\tau;t) = i\sum_{J_0M_0\varepsilon_0 i_0} w_{J_0}\int d\hat{R}\sum_{J\varepsilon i} C_{F_i}^{J_0M_0\varepsilon_0\,*}(J\varepsilon;t)\sum_{J'\varepsilon' i'} C_{F_{i'}}^{J_0M_0\varepsilon_0}(J'\varepsilon';t) \times \int d^3k\left\langle F_i;JM_0\varepsilon|\hat{\vec{\mu}}_{\rm el}\cdot\hat{\varepsilon}_{pr}|\vec{k};\hat{R}\right\rangle\int_0^\tau d\tau'\left\langle\vec{k}';\hat{R}|\hat{\vec{\mu}}_{\rm el}\cdot\vec{\varepsilon}_{pr}(\tau')|F_{i'};J'M_0\varepsilon'\right\rangle e^{-iS(\tau,\tau')} \tag{18}$$

with $S(\tau, \tau')$ being the time-dependent phase in the SFA. Eqn (18) has a transparent physical interpretation. The last two matrix elements encode the tunnel ionization initiating from state $|F_{i'};J'M_0\varepsilon'\rangle$ followed by a recombination to the state labeled $|F_i;JM_0\varepsilon\rangle$, whereas the coefficients $\{C_{F_i}^{J_0M_0\varepsilon_0}(J\varepsilon;t)\}$ contain the coupled rotational-electronic dynamics induced by the pump pulse. The completeness relation pertaining to the basis set $|JM\varepsilon;i\rangle$ enables one to project out the rotational degrees of freedom in $|F_i;JM\varepsilon\rangle$, thus arriving at a formal definition of a purely electronic factor that is a function of the electronic real-space coordinate $\{\vec{r}\}$ only

$$\left\langle\vec{r}\right|\otimes\left\langle J'M_0\varepsilon'|F_i;JM_0\varepsilon\right\rangle = \delta_{JJ'}\delta_{\varepsilon\varepsilon'}\left\langle\vec{r}|F_i^{J\varepsilon}\right\rangle. \tag{19}$$

This result allows one to decompose the matrix elements in eqn (18) into a rotational and an electronic factor

$$\left\langle F_i;JM_0\varepsilon|\hat{\vec{\mu}}_{\rm el}\cdot\hat{\varepsilon}_{pr}|\vec{k};\hat{R}\right\rangle = \left\langle F_i^{J\varepsilon}|\hat{\vec{\mu}}_{\rm el}\cdot\hat{\varepsilon}_{pr}|\vec{k}\right\rangle\left\langle JM_0\varepsilon;i|\hat{R}\right\rangle; \tag{20}$$

$$\left\langle\hat{R};\vec{k}'|\hat{\vec{\mu}}_{\rm el}\cdot\vec{\varepsilon}_{pr}(t)|F_i;JM_0\varepsilon\right\rangle = \left\langle\vec{k}'|\hat{\vec{\mu}}_{\rm el}\cdot\vec{\varepsilon}_{pr}(t)|F_i^{J\varepsilon}\right\rangle\left\langle\hat{R}|JM_0\varepsilon;i\right\rangle. \tag{21}$$

For a diatomic molecule with a single unpaired electron, the electronic part of the wavefunction $|F_i^{J\varepsilon}\rangle$ can be formulated in terms of the product $|\Phi_{\rm HOMO}\rangle e^{i\Lambda\chi_e}$, where $|\Phi_{\rm HOMO}\rangle$ is a function of all coordinates of the unpaired electron except the cylindrical azimuthal angle χ_e. The latter gives rise to an anisotropy in the electronic charge distribution as discussed in ref. 42. In this particular case, however,

the above anisotropy plays a negligible role since the low degrees of rotational excitation ensure the validity of the Hund's case a) limit. Thus the following approximation holds:

$$\left\langle F_1^{J\varepsilon}|\hat{\vec{\mu}}_{\mathrm{el}}\cdot\hat{\varepsilon}_{pr}|\vec{k}\right\rangle \simeq \left\langle F_2^{J\varepsilon}|\hat{\vec{\mu}}_{\mathrm{el}}\cdot\hat{\varepsilon}_{pr}|\vec{k}\right\rangle, \tag{22}$$

and the resulting expression for the dipole moment expectation value reads:

$$d(\tau;t) = i\sum_{J_0 M_0 \varepsilon_0 i_0} w_{J_0}\int d^3k\left\langle \Phi_{\mathrm{HOMO}}|\hat{\vec{\mu}}_{\mathrm{el}}\cdot\hat{\varepsilon}_{pr}|\vec{k}\right\rangle \times \int_0^{\tau} d\tau'\left\langle \vec{k}'|\hat{\vec{\mu}}_{\mathrm{el}}\cdot\vec{\varepsilon}_{pr}(\tau')|\Phi_{\mathrm{HOMO}}\right\rangle e^{-iS(\tau,\tau')}$$
$$\times\int d\hat{R}\sum_{J\varepsilon i} C_{F_i}^{J_0 M_0 \varepsilon_0 *}(J,\varepsilon;t)\left\langle JM_0\varepsilon;i|\hat{R}\right\rangle \sum_{J'\varepsilon' i'} C_{F_{i'}}^{J_0 M_0 \varepsilon_0}(J',\varepsilon';t)\left\langle \hat{R}|J'M_0\varepsilon';i'\right\rangle. \tag{23}$$

By defining a density matrix in Euler-angle space

$$\rho_{\mathrm{p}}(\hat{R},t) = \sum_{J\varepsilon i} C_{F_i}^{J_0 M_0 \varepsilon_0 *}(J,\varepsilon;t)\left\langle JM_0\varepsilon;i|\hat{R}\right\rangle \sum_{J'\varepsilon' i'} C_{F_{i'}}^{J_0 M_0 \varepsilon_0}(J',\varepsilon';t)\left\langle \hat{R}|J'M_0\varepsilon';i'\right\rangle \tag{24}$$

one obtains for eqn (23)

$$d(\tau;t) = \int d\hat{R}\rho_{\mathrm{p}}(\hat{R},t)\vec{D}(\hat{R},\tau), \tag{25}$$

wherein

$$\vec{D}(\hat{R},t) = i\int d^3k\left\langle \Phi_{\mathrm{HOMO}}|\hat{\vec{\mu}}_{\mathrm{el}}\cdot\hat{\varepsilon}_{pr}|\vec{k}\right\rangle \int_0^{\tau} d\tau'\left\langle \vec{k}'|\hat{\vec{\mu}}_{\mathrm{el}}\cdot\vec{\varepsilon}_{pr}(\tau')|\Phi_{\mathrm{HOMO}}\right\rangle e^{-iS(\tau,\tau')} \tag{26}$$

is the dipole-moment expectation value evaluated over a single pure state as defined in eqn (14) and (15). Consequently, $\rho_{\mathrm{p}}(\hat{R},t)$ can be interpreted as a factor that weights the contribution of each of the electronic integrals determining $\vec{D}(\hat{R},\tau)$ for a given molecular orientation $\hat{R}$. The calculations described in what follows were done by replacing the SFA expressions for strong-field ionization and photorecombination in eqn (26) with the strong-field ionization rate from ref. 39 and the photorecombination matrix elements described in Section 2.4. In order to arrive at a final expression for the harmonic intensity as a function of the pump–probe delay, the expressions in eqn (15) and (25) have to be integrated over all possible molecular orientations. This operation is straightforward in case the polarizations of the pump and the probe pulses coincide, and one obtains for the harmonic intensity $I(\omega,t)$

$$I(\omega,t) = \left|\int_0^{\pi}\sin\theta d\theta\rho_{\mathrm{p}}(\hat{R},t)\vec{D}_{\parallel}(\hat{R},t)\right|^2. \tag{27}$$

The treatment of the case where pump and probe polarizations differ requires the introduction of an additional system of variables (θ', ϕ') denoting the polar and the azimuthal angles of the molecular axis in a frame attached to the probe field.[43] The latter pair of variables is related to the polar and azimuthal angles

attached to the pump-pulse frame and the angle between the two polarizations α by

$$\cos\theta = \cos\theta'\cos\alpha + \sin\theta'\sin\alpha\cos\phi'. \quad (28)$$

The intensity of the emitted high-harmonic radiation can be obtained by evaluating

$$I(\omega, t, \alpha) = \left| \int_0^{2\pi} d\phi' \int_0^{\pi} \sin\theta' d\theta' \vec{D}_{\parallel}(\hat{R}, t)\rho_{\mathrm{p}}(\theta\{\phi', \theta'; \alpha\}, t) \right|^2 + \\ + \left| \int_0^{2\pi} d\phi' \cos\phi' \int_0^{\pi} \sin\theta' d\theta' \vec{D}_{\perp}(\hat{R}, t)\rho_{\mathrm{p}}(\theta\{\phi', \theta'; \alpha\}, t) \right|^2. \quad (29)$$

3 Experimental

The experimental setup consists of an amplified femtosecond titanium:sapphire laser system (10 mJ, 25 fs, 1 kHz, 800 nm center wavelength), an optical setup and a vacuum chamber for generation and spectral characterization of high-harmonic radiation. The output of the laser system is split into multiple beams. One of the pulses (pump, 60 fs) prepares the coupled electronic-rotational wave packet in NO through impulsive Raman scattering, while the other part (probe, 30 fs) is used to generate high-harmonic radiation with a cut-off at harmonic 27 ($\sim$ 42 eV). A translation stage is employed to control the temporal delay between the pump and the probe pulses. The two pulses impinge on a spherical mirror with a vertical offset of 7 mm and are focused non-collinearly into the molecular beam inside a vacuum chamber. The molecular beam is generated by an expansion of a 5% mixture of NO in He through a pulsed valve with a backing pressure of 9 bars. The total ion yield is measured by recording the electrical current flowing through a wire mesh placed 15 cm below the orifice of the valve and held at a relative potential of -1 kV. The peak intensity of the pump beam was varied in the range $(3.2 \pm 0.3) \times 10^{13}$ W cm^{-2} $-$ $(6.0 \pm 0.5) \times 10^{13}$ W cm^{-2}, whereas typical values for the probe intensity span the range $(1.0 \pm 0.2) \times 10^{14}$ W cm^{-2} $-(1.5 \pm 0.2) \times 10^{14}$ W cm^{-2}. The polarization of the probe beam is kept unchanged, whereas that of the pump beam is varied. The high-harmonic radiation generated by the probe beam propagates into an extreme-ultraviolet (XUV) spectrometer consisting of a 250 μm wide entrance slit, a concave aberration-corrected grating (Shimadzu, 30–002), and a microchannel-plate detector backed with a phosphor screen. The spectral images are recorded by a charge-coupled device camera and subsequently sent to a computer for analysis.

4 Results and discussion

4.1 Electronic wave packets probed by strong-field ionization and high-harmonic generation

We now discuss strong-field ionization and high-harmonic generation from a coherent superposition of electronic states. In Fig. 1a, we show the total strong-field ionization yield as a function of the pump–probe delay for a situation where

the polarizations of the two beams coincide (green curve) or are orthogonal to each other (orange curve). The harmonic intensity, integrated over harmonic orders 9 to 23 ($H9 - H23$), is shown in Fig. 1b for the two different polarization configurations. In both excitation schemes, the electronic wave packet prepared by the excitation pulse translates into a modulation with a period of $T = \frac{h}{\Delta E_{SO}} \approx 275$ fs, commensurable with the energy difference ΔE_{SO} between the F_1 and F_2 components. Comparing the ionization yield with the harmonic intensity, we find that the modulation depth increases by a factor of ≈ 4 in the latter case. In order to explain this behaviour, we next focus on the characteristic features of each probing mechanism.

Fig. 1 illustrates strong-field ionization (panel (*c*)) or high-harmonic generation (panel (*d*)) from the superposition state $\Psi = |c_1|e^{i\phi_1}\psi_1 + |c_2|e^{i\phi_2}\psi_2$, where ψ_1 and ψ_2 denote total normalized wave functions. Since the two initial states have nearly identical electronic structures and are separated by much less than the energy of one photon, the total strong-field ionization yield Y is given by the coherent sum of two contributions S_1 and S_2 as $Y \propto \left||c_1|e^{i\phi_1}S_1 + |c_2|e^{i\phi_2}S_2\right|^2$. The high-harmonic yield comprises contributions from four different channels, represented by

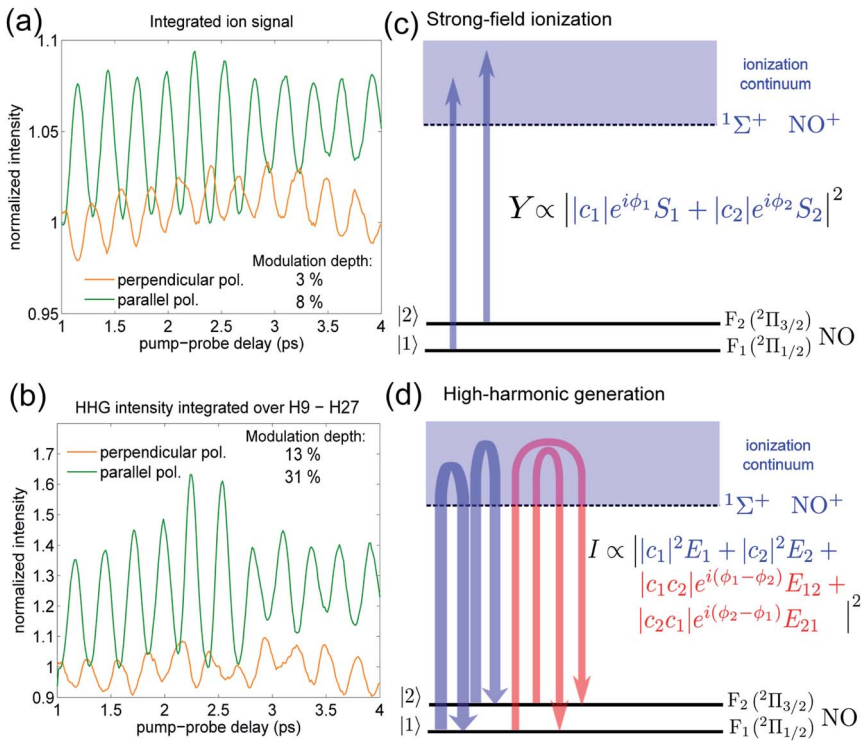

Fig. 1 Strong-field ionization (a) and high-harmonic generation (b) signals from a coherent superposition of F_1 and F_2 electronic states in NO. The plots on the left-hand side show normalized intensities from experiments featuring parallel (green) or crossed (orange) polarizations. The schemes on the right-hand side illustrate the quantum pathways contributing to the observed signals. Panel (d) has been adapted from ref. 9.

arrows in Fig. 1d.[9] The two channels (blue arrows) corresponding to ionization followed by recombination to the same state are sensitive only to the populations of the two states ($|c_1|^2$ and $|c_2|^2$) but not to their quantum phases. Conversely, the two red channels are sensitive to the initial phases and encode their difference in the phase of the emitted radiation. The total intensity of the emitted electric field can be decomposed as a sum of four different contributions as[9]

$I \propto \left||c_1|^2 E_1 + |c_2|^2 E_2 + |c_1 c_2| e^{i(\phi_1-\phi_2)} E_{12} + |c_1 c_2| e^{i(\phi_2-\phi_1)} E_{21}\right|^2$. For the same reasons as mentioned above, one can assume $E_1 \sim E_2 \sim E_{12} \sim E_{21}$. Comparing the expressions for Y and I, we find that the latter is formally similar to the former but is squared once more. This explains the observed higher sensitivity of HHG to the electronic dynamics.

Further, a comparison of the two polarization geometries reveals that the ionization yield as well as the harmonic intensity in the experiment with crossed polarizations display a smaller modulation depth and are shifted in phase by $\sim\pi$ with respect to the parallel configuration. In Fig. 2b we plot the temporal evolution of the harmonic intensity for several harmonic orders (H11-H15), calculated using the theoretical model discussed in section 2. Comparing the calculated results with the experimental data shown Fig. 2a reveals that our theory correctly captures both the different modulation depths and the phase shift between the two configurations. These two aspects encode the temporal evolution of the electronic wave packet, which corresponds to a valence-shell electron current flowing around the internuclear axis.[9] The calculation slightly overestimates the

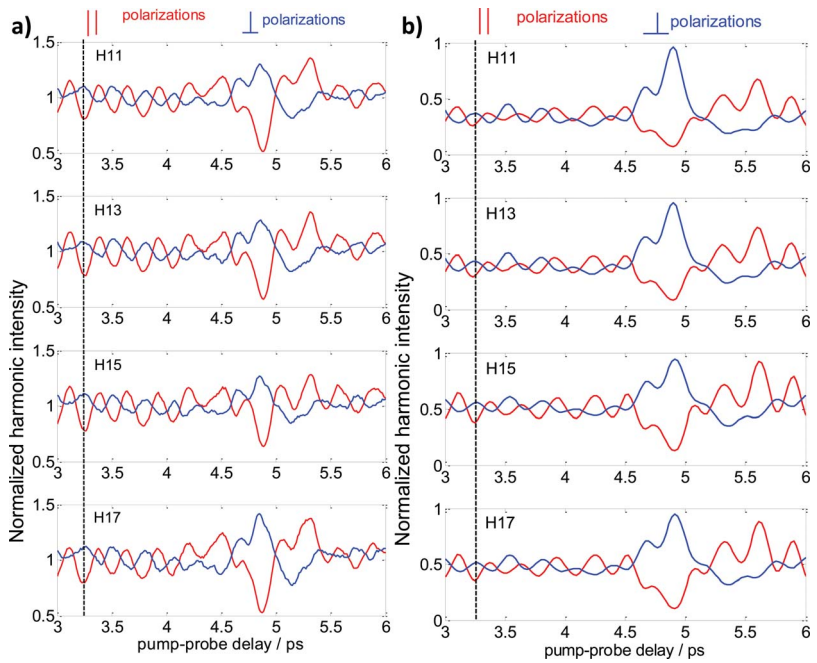

Fig. 2 High-harmonic intensities observed (a) and calculated (b) for different harmonic orders for parallel (red) or perpendicular (blue) polarizations. Note the different vertical scale used in the left and the right panels. The calculation was performed assuming a peak intensity of 4.5×10^{13} W cm^{-2} and a pulse duration of 60 fs for the pump pulse.

modulation depths but is in excellent overall agreement with the experiment. The modulation depth of both the rotational and the electronic modulations is highly sensitive to the parameter γ in eqn (9). The remaining discrepancy between experiment and theory suggests that the empirical value[38] for γ may not be very accurate.

4.2 HHG and SFI as probes of coupled electronic-rotational motion

Fig. 3a and c show the signal intensity as a function of the pump–probe delay for harmonic orders 9 and 15, respectively, whereas panels c) and d) show the Fourier transforms of the signals in the frequency domain. In harmoinc 9, the rotational dynamics manifests itself as a pattern of regularly spaced revival structures, recurring with a period of $\sim$5 ps that corresponds to the revival time of the molecular alignment. An additional signature of the rotational motion is the fractional revival feature that is discernible at each quarter revival time, as is typical of molecules with a π-symmetry HOMO. The maximum (minimum) of the revival structure correspond to the time delays when the wave packet is strongly localized in angular space, either parallel to the axis defined by the pump polarization direction (or delocalized in the plane orthogonal to it). Irregularities

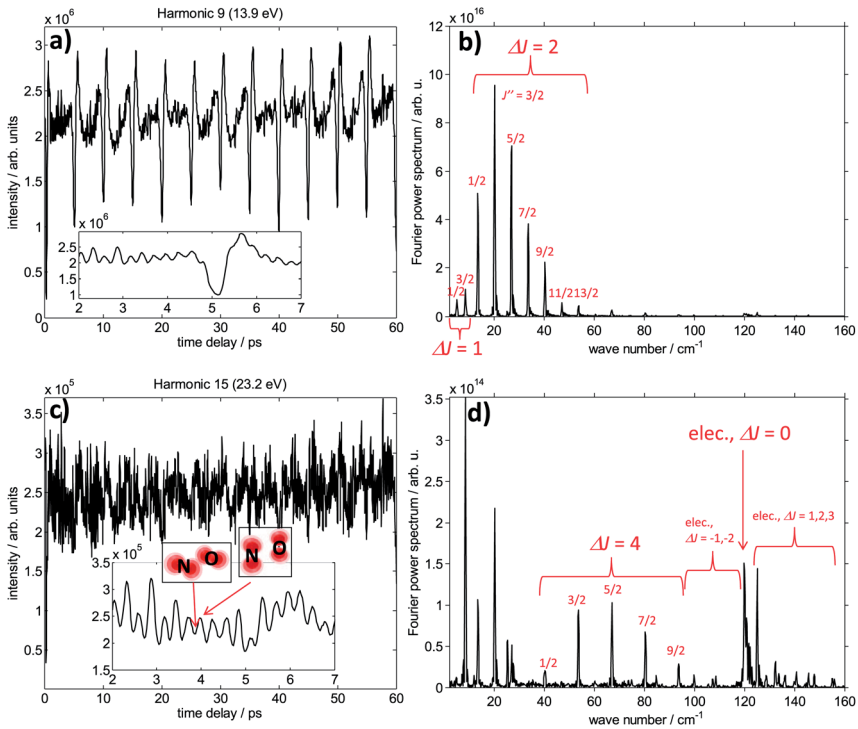

Fig. 3 High-harmonic intensities measured using parallel pump–probe polarizations in *H*9 (a) and *H*15 (c) and Fourier-transform power spectra (b and d). The observed coherences are assigned in terms of the angular momentum quantum number *J* of the lower-lying state, the change in rotational quantum number (ΔJ) and a possible change of electronic state (elec.).

in the signal at long delays hint at progressive dephasing of the electronic quantum beat due to the presence of incommensurate frequencies in the wave packet and coupling to molecular rotation.

The electronic coherence is revealed in the modulations that dominate the signal in between the rotational revivals. These oscillations, shown in the inset of Fig. 3a, represent the electronic beating with a period of $\sim 275 \pm 2$ fs, discussed in the preceding section. Both the pure rotational as well as the electronic coherences give rise to characteristic features in the frequency domain. As evident from the Fourier-transformed signals displayed in Fig. 3b, the rotational part of the spectrum consists of a cluster of peaks at low wavenumbers that correspond to pure rotational transitions within the F_1 state and is primarily dominated by contributions arising from exchange of two units of angular momentum ($\Delta J = \pm 2$). The electronic transition is present as a barely distinguishable structure around 120 cm^{-1}. Although similar qualitative arguments can be applied to the spectrum of harmonic 15, the suppression of the pure rotational coherences constitutes a striking difference. As emphasized in the inset of panel *c*), oscillations arising from the electronic coherence become comparable in amplitude to the rotational revival features, in contrast to the tendency observed in panels *a*) and *b*). Moreover, the pure rotational coherences are dominated by higher frequencies ($\Delta J = \pm 4$). The high wave-number part of the spectrum is dominated

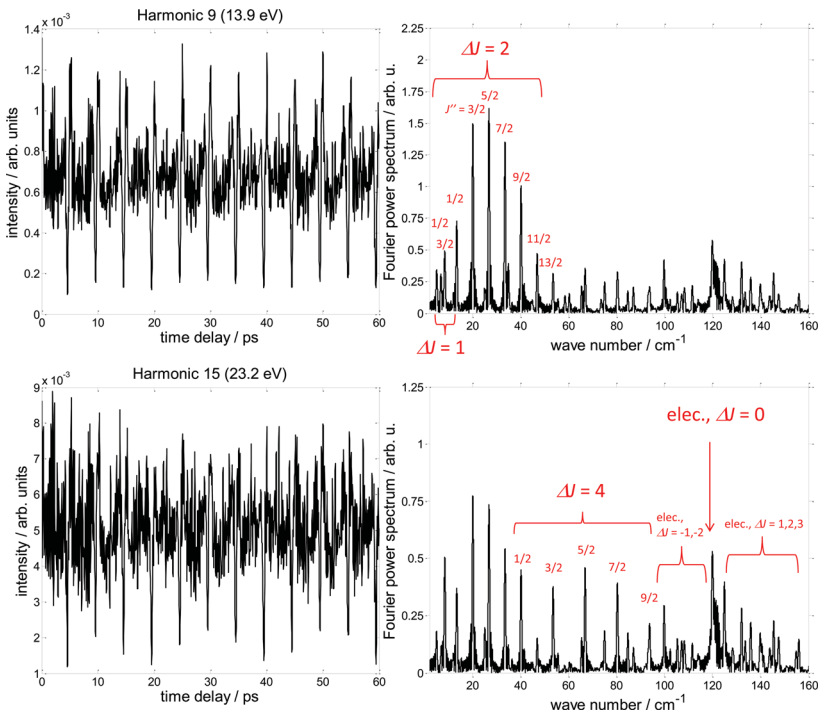

Fig. 4 Calculated high-harmonic intensities for *H*9 and *H*15 using a 60 fs pump pulse with a peak intensity of 4.8×10^{13} W cm^{-2}, matching the experimental data shown in Fig. 3. Panels (a) and (c) correspond to the time-domain signals of *H*9 and *H*15, respectively. The Fourier-transform power spectra are shown in panels (c) and (d).

by the electronic coherence as well as mixed electronic-rotational transitions ($\Delta J = \pm 1, \pm 2$).

The calculated intensities in both time and frequency domains for harmonic orders 9 and 15 are depicted in Fig. 4. Our model reproduces the main observations such as the increasing importance of the electronic coherences and high-order pure rotational Raman transitions when proceeding from *H*9 to *H*15. However, the calculations tend to overestimate the relative strength of the electronic and mixed coherences in *H*9 and predict a different intensity distribution in *H*15.

For the purpose of comparison, an analogous frequency-domain analysis has been performed on the experimental total ion yield as a function of time (Fig. 5a). The Fourier spectrum of the total ion yield depicted in Fig. 5b reveals the presence of both pure rotational as well as electronic or mixed electronic-rotational excitations. Interestingly, the electronic and mixed coherences strongly dominate over the purely rotational coherences, which is in contrast to the high-harmonic yields. Strong-field ionization is thus found to be relatively more sensitive to electronic rather than rotational motion in NO, while the opposite is true for HHG.

We thus conclude that while harmonic 9 is most sensitive to rotational motion, harmonics of order 15 (and higher) are more sensitive to the electronic motion. This observation might be a general effect because the near-treshold region in photoionization is usually rich in continuum resonances which can cause a strong angular dependence of the photoionization cross section and thus give rise to a strong angle-dependence of the harmonic signal. In the remaining part of the current section, we investigate the mechanisms underlying the sensitivity of different harmonic orders to rotational dynamics. In order to explain the observations reported in the preceding text, we show in Fig. 6a the partial photoionization cross section for an electron ejected along the positive z-direction defined by the polarization of the photoionizing radiation and leaving NO^+ in its $^1\Sigma^+$ ground electronic state, as a function of both the alignment angle and the photon energy. An alignment angle of 0 degrees corresponds to the oxygen atom lying on the positive z axis. Along the photon-energy axis we observe a sharp local

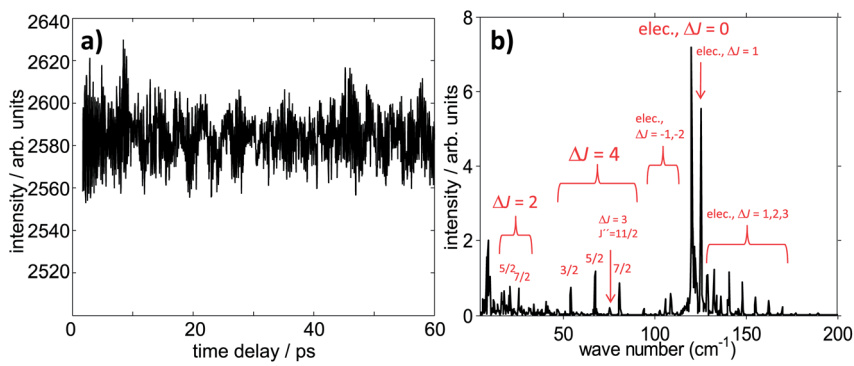

Fig. 5 Measured variation of the total ion yield as a function of the pump–probe delay (a) and Fourier-transform power spectrum (b) with coherences labeled by the corresponding change in rotational angular momentum quantum number (ΔJ) and a possible change in electronic state (F_1 to F_2).

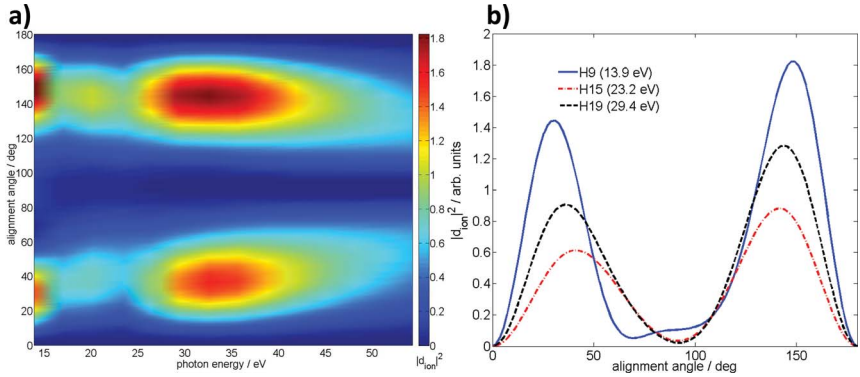

Fig. 6 (a): Calculated molecular-frame photoionization cross section for photoemission along the polarization of the ionizing radiation as a function of the photon energy and alignment angle. (b) Photoionization cross section corresponding to selected harmonic orders as a function of the alignment angle.

maximum close to 14 eV, a minimum close to 23 eV and a subsequent broad maximum in the range of 30–35 eV. The first maximum is caused by the presence of several resonances in the photoionization continuum of the $X^1\Sigma^+$ state. The region of 13–17 eV contains at least two valence autoionizing resonances ($4\sigma \rightarrow 2\pi$) and ($1\pi \rightarrow 2\pi$), in addition to a 3–4 eV broad ($\sigma \rightarrow \sigma^*$) shape resonance.[41] The second broad maximum in the range of 30–35 eV is caused by interchannel coupling to shape resonances in the $(4\sigma)^{-1}$ and $(5\sigma)^{-1}$ channels.

We now turn to the angular dependence of the photoionization cross section. Fig. 6b highlights the angular dependence of three harmonic orders (*H*9, *H*15 and *H*19). The photoionization cross section corresponding to the photon energy of *H*9 exhibits a pronounced variation with alignment angle, which can again be attributed to the presence of the resonances mentioned in the last paragraph. In contrast, the amplitude of *H*15 varies more weakly with the alignment angle. This theoretical result rationalizes the experimental observation from Fig. 3, *i.e.* the fact that H9 is much more sensitive to the rotational dynamics than H15.

The maxima and minima in the photoionization cross section of Fig. 6a are also reflected in the spectral amplitude of the individual harmonic orders. Fig. 7a shows an experimental high-harmonic spectrum emitted from aligned NO molecules and Fig. 7b shows the intensities of all harmonic orders on a linear scale. The spectral amplitude exhibits a maximum at *H*9 and a local minimum at *H*15. These features are also reproduced in the high-harmonic spectrum calculated according to eqn (15) (using $W(\omega) = 1$ and averaging over the calculated axis distribution) which is shown in panel *c*). This observation corroborates the fact that structures of photoionization continua such as Cooper minima[31] or shape resonances[44–46] become observable in high-harmonic spectra even when they arise through inter-channel coupling as in the case of the giant resonance in xenon.[47,48]

4.3 Intensity scaling

Next, we exploit the sensitivity of HHG to rotational or mixed electronic-rotational motion to study the influence of the pump intensity. As is evident from Fig. 8a–c, which shows the Fourier transform of *H*11 at three different pump intensities,

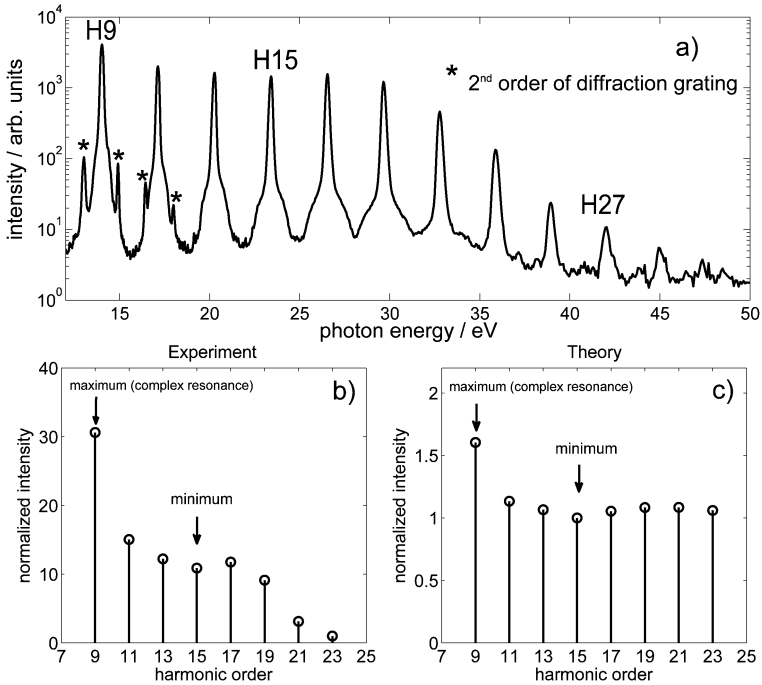

Fig. 7 Observed high-harmonic spectrum at a pump–probe delay corresponding to maximal alignment (5.25 ps, panel (a)), extracted intensity stick spectrum (b) and calculated high-harmonic stick spectrum (c). The decreasing intensity of harmonic orders above 21 (cutoff region) in panel (c) is not reproduced in the calculations because the spectral amplitude of the electron wave packet has been set to unity.

increasing the pump intensity leads to an enhancement of the electronic coherence, whose spectral signature is present as the pronounced peak at $\sim$120 cm^{-1}. Simultaneously, higher pump intensities permit the observation of weak spectral signatures associated with mixed electronic-rotational coherences. Remarkably, the pure rotational Raman transitions follow a different trend. While increasing the pump beam intensity from 3.2×10^{13} W cm^{-2} to 4.8×10^{13} W cm^{-2} stimulates the rotational Raman process, as evident in Fig. 8b and c, a further increase results in an observable decay. Concomitantly, the rotational distribution becomes broader due to consecutive Raman excitations. Thus, we may conclude that an increase of the pump intensity favors the electronic Raman scattering process and leads to a more effective population transfer from the F_1 to the F_2 state while rotational Raman transitions within the F_1 manifold are saturated at lower excitation energies. In Fig. 8d–f, the pump intensity scaling is studied theoretically by solving the time-dependent Schrödinger equation of the system with the methods outlined in Section 2. Although the model captures correctly the experimentally observed intensity dependence, it visibly overestimates the role of the higher-order Raman transitions while at the same time underestimating the growth of the electronic coherence. In particular, the predicted amplitudes of the mixed electronic-rotational coherences and rotational Raman transitions involving the exchange of four units of angular momentum ($\Delta J = 4$) are

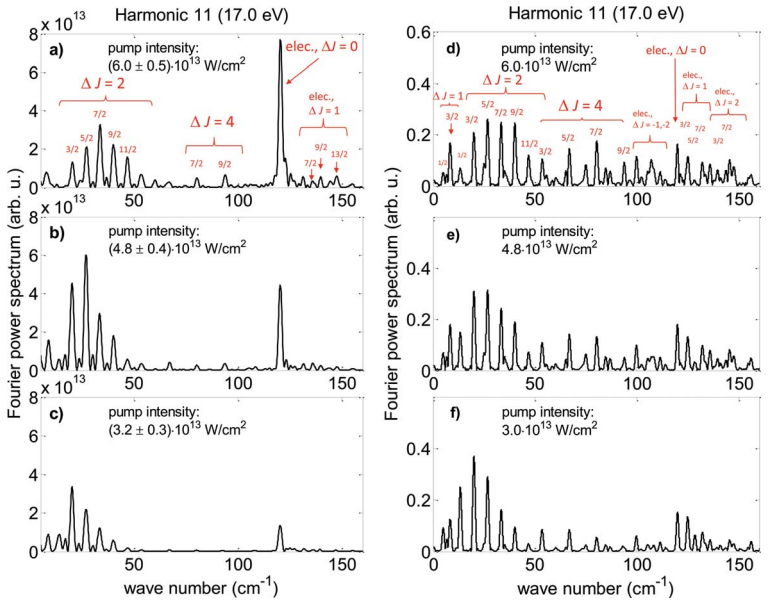

Fig. 8 a–c) Fourier-transform power spectra of experimental pump–probe signals of *H*11 measured under parallel pump–probe polarizations using different peak intensities of the pump pulse. d–f) Fourier-transform spectra of the calculated high-harmonic intensity of *H*11 with laser-pulse parameters matching the experimental data shown in a–c.

overestimated with respect to the experimental observations. In addition, the predicted intensity profile of the mixed electronic-rotational coherences is much broader than actually observed. These discrepancies indicate avenues for improving our theory.

5 Conclusions

We have studied a coupled electronic and rotational wave packet by high-harmonic spectroscopy and strong-field ionization. High-harmonic generation from a coherent superposition of electronic states was found to be ~4 times more sensitive to the electronic coherence than SFI. This result can be rationalized as being the consequence of two interfering pathways in the case of SFI and four pathways in the case of HHS. Although high-harmonic generation is usually considered to be a parametric process that leaves the target molecule in the initial quantum state, our experiment clearly demonstrates the existence of inelastic pathways for high-harmonic generation which enable the detection of electronic coherence. We further showed that different high-harmonic orders present a very different relative sensitivity to rotational or electronic motion in NO, while strong-field ionization is most sensitive to the electronic motion.

A theoretical description of HHS for coupled electronic and nuclear dynamics has been developed that quantitatively accounts for most experimental observations. It correctly predicts the detection of purely rotational, purely electronic and mixed coherences. Our theory further explains the surprisingly different sensitivities of different harmonic orders to rotational or electronic dynamics. The

origin of this sensitivity is shown to lie in the angular variation of photo-recombination dipole moments which is strongly modified by the presence of an autoionizing and shape resonances in the photoionization continuum of NO at a photon energy of ~14 eV.

The technique introduced in ref. 9 and developed further in the present work demonstrates the potential of HHS to the probing of extremely weak electronic coherences and the study of electronic dynamics that is strongly coupled to nuclear motion. These are key features unique to HHS that are valuable for studying excited-state dynamics in polyatomic molecules. The present technique will readily extend to studying few-femtosecond to attosecond dynamics when few-cycle carrier-envelope-phase-stable laser pulses are used. It will also benefit from recent progress in molecular orientation[44,49,50] which will enable studies of the spatial asymmetries of electronic wave packets.

Acknowledgements

We gratefully acknowledge funding from the Swiss National Science Foundation (PP00P2_128274). We thank R. R. Lucchese for providing the photoionization matrix elements displayed in Fig. 6.

References

1 M. Drescher, M. Hentschel, M. Uiberacker, V. Yakovlev, S. A., T. Westerwalbesloh, U. Heinzmann and F. Krausz, *Nature*, 2002, **419**, 803–807.
2 M. Schultze, M. Fie, N. Karpowicz, J. Gagnon, M. Korbman, M. Hofstetter, S. Neppl, A. L. Cavalieri, Y. Komninos, T. Mercouris, C. A. Nicolaides, R. Pazourek, S. Nagele, J. Feist, J. Burgdörfer, A. M. Azzeer, R. Ernstorfer, R. Kienberger, U. Kleineberg, E. Goulielmakis, F. Krausz and V. S. Yakovlev, *Science*, 2010, **328**, 1658–1662.
3 J. Mauritsson, P. Johnsson, E. Mansten, M. Swoboda, T. Ruchon, A. L'Huillier and K. J. Schafer, *Phys. Rev. Lett.*, 2008, **100**, 073003.
4 E. Goulielmakis, Z.-H. Loh, A. Wirth, R. Santra, N. Rohringer, V. S. Yakovlev, S. Zherebtsov, T. Pfeifer, A. M. Azzeer, M. F. Kling, S. R. Leone and F. Krausz, *Nature*, 2010, **466**, 739–743.
5 C. Ott, A. Kaldun, P. Raith, K. Meyer, M. Laux, J. Evers, C. H. Keitel, C. H. Greene and T. Pfeifer, *Science*, 2013, **340**, 716–720.
6 J. Herrmann, M. Weger, R. Locher, M. Sabbar, P. Rivière, U. Saalmann, J.-M. Rost, L. Gallmann and U. Keller, *Phys. Rev. A: At., Mol., Opt. Phys.*, 2013, **88**, 043843.
7 H. J. Wörner and P. B. Corkum, *J. Phys. B: At., Mol. Opt. Phys.*, 2011, **44**, 041001.
8 A. Fleischer, H. J. Wörner, L. Arissian, L. R. Liu, M. Meckel, A. Rippert, R. Dörner, D. M. Villeneuve, P. B. Corkum and A. Staudte, *Phys. Rev. Lett.*, 2011, **107**, 113003.
9 P. M. Kraus, S. B. Zhang, A. Gijsbertsen, R. R. Lucchese, N. Rohringer and H. J. Wörner, *Phys. Rev. Lett.*, 2013, **111**, 243005.
10 T. Millack and A. Maquet, *J. Mod. Opt.*, 1993, **40**, 2161–2171.
11 F. I. Gauthey, C. H. Keitel, P. L. Knight and A. Maquet, *Phys. Rev. A: At., Mol., Opt. Phys.*, 1995, **52**, 525–540.

12 J. B. Watson, A. Sanpera, X. Chen and K. Burnett, *Phys. Rev. A: At., Mol., Opt. Phys.*, 1996, **53**, R1962–R1965.
13 H. Niikura, D. M. Villeneuve and P. B. Corkum, *Phys. Rev. Lett.*, 2005, **94**, 083003.
14 H. J. Wörner, J. B. Bertrand, D. V. Kartashov, P. B. Corkum and D. M. Villeneuve, *Nature*, 2010, **466**, 604–607.
15 H. J. Wörner, J. B. Bertrand, B. Fabre, J. Higuet, H. Ruf, A. Dubrouil, S. Patchkovskii, M. Spanner, Y. Mairesse, V. Blanchet, E. Mével, E. Constant, E. Constant, P. B. Corkum and D. M. Villeneuve, *Science*, 2011, **334**, 208–212.
16 P. M. Kraus, Y. Arasaki, J. B. Bertrand, S. Patchkovskii, P. B. Corkum, D. M. Villeneuve, K. Takatsuka and H. J. Wörner, *Phys. Rev. A: At., Mol., Opt. Phys.*, 2012, **85**, 043409.
17 P. M. Kraus and H. J. Wörner, *Chem. Phys.*, 2013, **414**, 32–44.
18 A. Tehlar and H. J. Wörner, *Mol. Phys.*, 2013, **111**, 2057–2067.
19 O. Smirnova, Y. Mairesse, S. Patchkovskii, N. Dudovich, D. Villeneuve, P. Corkum and M. Y. Ivanov, *Nature*, 2009, **460**, 972–977.
20 S. Haessler, J. Caillat, W. Boutu, C. Giovanetti-Teixeira, T. Ruchon, T. Auguste, Z. Diveki, P. Breger, A. Maquet, B. Carre, R. Taieb and P. Salières, *Nat. Phys.*, 2010, **6**, 200–206.
21 A. Rupenyan, P. M. Kraus, J. Schneider and H. J. Wörner, *Phys. Rev. A: At., Mol., Opt. Phys.*, 2013, **87**, 033409.
22 A. Rupenyan, P. M. Kraus, J. Schneider and H. J. Wörner, *Phys. Rev. A: At., Mol., Opt. Phys.*, 2013, **87**, 031401.
23 S. Ramakrishna and T. Seideman, *Phys. Rev. Lett.*, 2007, **99**, 113901.
24 S. Ramakrishna and T. Seideman, *Phys. Rev. A: At., Mol., Opt. Phys.*, 2008, **77**, 053411.
25 S. Ramakrishna, P. A. J. Sherratt, A. D. Dutoi and T. Seideman, *Phys. Rev. A: At., Mol., Opt. Phys.*, 2010, **81**, 021802.
26 A. Abdurrouf and F. H. M. Faisal, *Phys. Rev. A: At., Mol., Opt. Phys.*, 2009, **79**, 023405.
27 F. H. M. Faisal, A. Abdurrouf, K. Miyazaki and G. Miyaji, *Phys. Rev. Lett.*, 2007, **98**, 143001.
28 F. H. M. Faisal and A. Abdurrouf, *Phys. Rev. Lett.*, 2008, **100**, 123005.
29 A.-T. Le, R. R. Lucchese, S. Tonzani, T. Morishita and C. D. Lin, *Phys. Rev. A: At., Mol., Opt. Phys.*, 2009, **80**, 013401.
30 T. Morishita, A.-T. Le, Z. Chen and C. D. Lin, *Phys. Rev. Lett.*, 2008, **100**, 013903.
31 H. J. Wörner, H. Niikura, J. B. Bertrand, P. B. Corkum and D. M. Villeneuve, *Phys. Rev. Lett.*, 2009, **102**, 103901.
32 A.-T. Le, R. R. Lucchese and C. D. Lin, *Phys. Rev. A: At., Mol., Opt. Phys.*, 2013, **87**, 063406.
33 J. M. Brown and A. Carrington, *Rotational Spectroscopy of Diatomic Molecules*, Cambridge University Press, 1st edn, 2003.
34 R. N. Zare, *Angular Momentum: Understanding Spatial Aspects in Chemistry and Physics*, John Wiley & and Sons, 1st edn, 1988.
35 A. R. Edmonds, *Angular Momentum in Quantum Mechanics*, Princeton University Press, 1st edn, 1957.
36 J. H. Van Vleck, *Rev. Mod. Phys.*, 1951, **23**, 213–227.
37 P. U. Manohar and S. Pal, *Chem. Phys. Lett.*, 2007, **438**, 321–325.
38 D. W. Lepard, *Can. J. Phys.*, 1970, **48**, 1664–1674.

39 H. Li, D. Ray, S. De, I. Znakovskaya, W. Cao, G. Laurent, Z. Wang, M. F. Kling, A. T. Le and C. L. Cocke, *Phys. Rev. A: At., Mol., Opt. Phys.*, 2011, **84**, 043429.
40 R. R. Lucchese, G. Raseev and V. McKoy, *Phys. Rev. A: At., Mol., Opt. Phys.*, 1982, **25**, 2572–2587.
41 R. E. Stratmann, R. W. Zurales and R. R. Lucchese, *J. Chem. Phys.*, 1996, **104**, 8989–9000.
42 M. H. Alexander and J. Dagdigian, *J. Chem. Phys.*, 1984, **80**, 4325.
43 M. Lein, R. De Nalda, E. Heesel, N. Hay, E. Springate, R. Velotta, M. Castillejo, P. L. Knight and J. P. Marangos, *J. Mod. Opt.*, 2005, **52**, 465–478.
44 A. Rupenyan, J. B. Bertrand, D. M. Villeneuve and H. J. Wörner, *Phys. Rev. Lett.*, 2012, **108**, 033903.
45 X. Ren, V. Makhija, A.-T. Le, J. Troß, S. Mondal, C. Jin, V. Kumarappan and C. Trallero-Herrero, *Phys. Rev. A: At., Mol., Opt. Phys.*, 2013, **88**, 043421.
46 P. Kraus, D. Baykusheva and H. J. Worner, *Phys. Rev. Lett.*, 2014, **113**, 023001.
47 A. D. Shiner, B. Schmidt, C. Trallero-Herrero, H. J. Wörner, S. Patchkovskii, P. B. Corkum, J.-C. Kieffer, F. Légaré and D. M. Villeneuve, *Nat. Phys.*, 2011, **7**, 464–467.
48 S. Pabst and R. Santra, *Phys. Rev. Lett.*, 2013, **111**, 233005.
49 P. M. Kraus, A. Rupenyan and H. J. Wörner, *Phys. Rev. Lett.*, 2012, **109**, 233903.
50 P. M. Kraus, D. Baykusheva and H. J. Wörner, *J. Phys. B: At. Mol. Opt. Phys.*, 2014, **47**, 124030.

